

Refining Heuristic Predictors of Fractional Chern Insulators using Machine Learning

Oriol Mayné i Comas^{★,1,2} André Grossi Fonseca^{★,1,3,*} Sachin Vaidya^{1,3,4,†} and Marin Soljačić^{1,3,4}

¹*Department of Physics, Massachusetts Institute of Technology, Cambridge, Massachusetts 02139, USA*

²*Universitat Politècnica de Catalunya, Barcelona 08034, Spain*

³*The NSF Institute for Artificial Intelligence and Fundamental Interactions*

⁴*Research Laboratory of Electronics, Massachusetts Institute of Technology, Cambridge, Massachusetts 02139, USA*

[★] denotes equal contribution

We develop an interpretable, data-driven framework to quantify how single-particle band geometry governs the stability of fractional Chern insulators (FCIs). Using large-scale exact diagonalization, we evaluate an FCI metric that yields a continuous spectral measure of FCI stability across parameter space. We then train Kolmogorov–Arnold networks (KANs)—a recently developed interpretable neural architecture—to regress this metric from two band-geometric descriptors: the trace violation T and the Berry curvature fluctuations σ_B . Applied to spinless fermions at filling $\nu = 1/3$ in models on the checkerboard and kagome lattices, our approach yields compact analytical formulas that predict FCI stability with over $> 80\%$ accuracy in both regression and classification tasks, and remain reliable even in data-scarce regimes. The learned relations reveal model-dependent trends, clarifying the limits of Landau-level-mimicking heuristics. Our framework provides a general method for extracting simple, phenomenological “laws” that connect many-body phase stability to chosen physical descriptors, enabling rapid hypothesis formation and targeted design of quantum phases.

I. INTRODUCTION

Fractional quantum Hall (FQH) physics constitutes a striking example of emergence and topological order in many-body physics. In two-dimensional (2D) electron gases with partially filled lowest Landau level (LL), the holomorphic structure of single-particle wavefunctions enables precise analytical descriptions, such as ansatz wavefunctions [1] and exact pseudopotential arguments [2–4]. The discovery of fractional Chern insulators (FCIs) [5–14] extended this physics to lattice systems without magnetic fields, where topologically ordered states arise from partially filled Chern bands. Recent experiments in moiré superlattices [15–28] have provided compelling evidence for the existence of such states.

However, partially filling a nearly flat Chern band alone does not guarantee an FCI ground state. Recently, the role of single-particle band geometry in stabilizing FCIs has been elucidated [5, 7, 29–40]. In particular, two geometric quantities have been found to be the most relevant: the “trace violation” T , which quantifies deviations from the lowest LL relation between the Fubini–Study metric and Berry curvature; and the Brillouin zone fluctuations of the Berry curvature σ_B . These metrics quantify similarities to the algebra of projected density operators in the lowest LL [29, 41], and their single-particle nature means they are computationally efficient surrogates for costly many-body computations. In practice, however, these quantities vary together, making it difficult to disentangle their individual roles or assess their predictive power. This lack of quantitative understanding limits both the interpretation of numerical results and the ability to design systems optimized for fractionalized ground states.

In this work, we take a step toward filling this gap by developing a data-driven approach to evaluate how well these geometric heuristics predict FCI stability. We use high-throughput exact diagonalization (ED) to evaluate the FCI quality [42] across parameter space, which is a continuous metric quantifying the stability of, or distance from, an FCI phase. We then employ Kolmogorov–Arnold networks (KANs) [43]—a symbolic, interpretable machine-learning (ML) architecture—to extract simple and accurate symbolic formulas, akin to phenomenological “laws” for how this quality metric depends on band geometry. We apply our pipeline to two prototypical tight-binding models for spinless fermions on the checkerboard and kagome lattices at filling $\nu = 1/3$. Strikingly, we find that simple formulas involving only T and σ_B predict FCI stability with over 80% accuracy in both regression and classification tasks. The learned relations also reveal model-dependent behavior: while large σ_B destabilizes the kagome FCI, it enhances stability in the checkerboard lattice, highlighting the limitations of heuristics that solely mimic LLs. Moreover, our approach remains suitable even in data-scarce regimes, accurately capturing these trends with as few as $\sim 10^2$ ED samples. Our results offer an interpretable framework for evaluating the stability of many-body quantum phases as a function of arbitrary physical quantities of interest.

This paper is organized as follows. In Section II, we describe the dataset, define the FCI quality metric, and detail the lattice models and band-geometric predictors. Section III reviews Kolmogorov–Arnold networks (KANs) and outlines the evaluation pipeline used to extract symbolic formulas. Section IV presents our main results, including representative formulas, model-dependent trends, and their physical interpretation. Finally, Section V concludes with discussions of our results and outlook.

* agfons@mit.edu

† svaidya1@mit.edu

II. BACKGROUND AND DATASET

A. Exact diagonalization and FCIs

In the exact diagonalization (ED) method, one directly constructs and computes the low-energy spectrum of a many-body Hamiltonian $H(\mathbf{p})$, typically a function of physical parameters \mathbf{p} . Numerical efficiency can be achieved by exploiting symmetries to block-diagonalize $H(\mathbf{p})$, in which each block corresponds to a symmetry sector and can therefore be labeled by quantum numbers \mathcal{K}_i . For example, in a 2D system with discrete translational symmetry, the components of the center-of-mass momentum along each primitive lattice vector are good quantum numbers. Consequently, the Hamiltonian can be constructed and diagonalized within each irreducible representation of the translation group. A typical ED spectrum then consists of eigenenergies as a function of discrete quantum numbers, $\{E_{\mathcal{K}_i}(\mathbf{p})\}$.

Although the Hilbert-space dimension within each sector grows exponentially with system size, this symmetry resolution greatly reduces the computational cost and provides insights into the ground state and excitation spectra, making ED an indispensable tool for strongly correlated systems. Due to the physics of FCIs being typically dominated by short-range correlations [1–4], FCI ground states can be resolved at modest system sizes, and therefore ED has been extensively employed to study their behavior. In finite clusters at fractional fillings, FCIs are identified in ED through a combination of signatures: a quasi-degenerate ground-state manifold separated by a clear spectral gap, a characteristic spectral flow under adiabatic flux insertion, and an entanglement gap and a peculiar level count in the particle-cut entanglement spectrum [6, 7]. Based on this numerical evidence, ED has been used to identify FCI ground states in a variety of lattices [8, 11–14, 44], as well as in models in the continuum [45–51].

B. FCI quality metric

We now introduce a metric that turns the low-energy spectrum $\{E_{\mathcal{K}_i}(\mathbf{p})\}$ of an ED calculation into a continuously varying stability measure for FCIs. For this, we employ a modified version of the recently introduced “target-phase loss function” [42], which we now briefly review.

Being topologically ordered phases, FCIs are known to display ground state degeneracy on a torus, which becomes a quasi-degeneracy due to finite-size splitting. The ground-state manifold can then be labeled by a set of symmetry sectors $\{\mathcal{K}_i^*\}$, with corresponding degeneracies $\{d_i^*\}$. For a particular FCI, the data $\{(\mathcal{K}_i^*, d_i^*)\}$ is known beforehand for any system size with $N_1 \times N_2$ unit cells along primitive lattice vectors [12, 52, 53]. Then, we split $\{E_{\mathcal{K}_i}(\mathbf{p})\}$ into two sets, which we call the target and complement manifolds. The former consists of the lowest d_i^* energy levels in each \mathcal{K}_i^* sector, and the latter comprises all

remaining energy levels. We now introduce the function

$$\tilde{\ell}(\mathbf{p}, \Phi) = \max_{E \in \text{target}} E(\mathbf{p}, \Phi) - \min_{E \in \text{complement}} E(\mathbf{p}, \Phi), \quad (1)$$

which, at a given threaded magnetic flux Φ , is simply the gap between the ground state energy of the complement manifold and the highest excited state energy in the target manifold. If $\tilde{\ell}(\mathbf{p}, \Phi) < 0$, then the system at point \mathbf{p} and flux Φ is in the target phase at \mathbf{p} with associated many-body gap $-\tilde{\ell}$. If $\tilde{\ell}(\mathbf{p}, \Phi) > 0$, the loss function encodes the spectral distance from an FCI ground state. We then ensure that the many-body gap stays open under adiabatic flux insertion [54] by defining

$$\tilde{\mathcal{L}}(\mathbf{p}) = \max_{\{\Phi_j\}} \tilde{\ell}(\mathbf{p}, \Phi_j), \quad (2)$$

where the maximum is taken over a finite user-defined sampling of flux values $\{\Phi_j\}$. Since the max function is negative if and only if all of its arguments are negative, $\tilde{\mathcal{L}}(\mathbf{p}) < 0$ signals that the many-body gap remains finite for every flux in the set $\{\Phi_j\}$.

These definitions provide an initial basis for defining the quality of ($\tilde{\mathcal{L}} < 0$) or distance from ($\tilde{\mathcal{L}} > 0$) an FCI ground state. However, the regime in which $\tilde{\ell}(\mathbf{p}, \Phi) < 0$ only contains information about the many-body gap. In practice, the quality of an FCI should also account for the energy spread of the ground state quasi-degeneracy, defined as

$$\delta(\mathbf{p}, \Phi) = \max_{E \in \text{target}} E(\mathbf{p}, \Phi) - \min_{E \in \text{target}} E(\mathbf{p}, \Phi), \quad (3)$$

with smaller values of $\delta(\mathbf{p}, \Phi)$ denoting more stable FCIs. However, note that it is not enough to simply take the ratio of Eq. (1) and Eq. (3), since $\delta(\mathbf{p}, \Phi)$ is not meaningful in the case where $\tilde{\ell}(\mathbf{p}, \Phi) > 0$. To ensure $\delta(\mathbf{p}, \Phi)$ is accounted for only when the ground state is an FCI, we divide $\tilde{\ell}$ by a function which smoothly interpolates between δ and unity when $\tilde{\ell}(\mathbf{p}, \Phi)$ goes from negative to positive. In particular, we choose

$$\ell(\mathbf{p}, \Phi) = \frac{\tilde{\ell}(\mathbf{p}, \Phi)}{\delta(\mathbf{p}, \Phi) + (1 - \delta(\mathbf{p}, \Phi)) \sigma(\tilde{\ell}(\mathbf{p}, \Phi)/\delta(\mathbf{p}, \Phi))}, \quad (4)$$

where $\sigma(x) = (1 + \exp(-x))^{-1}$ is the sigmoid function. Since $\sigma(x) \rightarrow 1, 0$ for $x \rightarrow \pm\infty$, $\ell(\mathbf{p}, \Phi) \rightarrow \tilde{\ell}(\mathbf{p}, \Phi)$ for large positive $\tilde{\ell}(\mathbf{p}, \Phi)$, but $\ell(\mathbf{p}, \Phi) \rightarrow \tilde{\ell}(\mathbf{p}, \Phi)/\delta(\mathbf{p}, \Phi)$ for large negative $\tilde{\ell}(\mathbf{p}, \Phi)$, on the scale of the spread, as desired. Finally, we define the FCI quality metric to be

$$\mathcal{L}(\mathbf{p}) = \max_{\{\Phi_j\}} \ell(\mathbf{p}, \Phi_j). \quad (5)$$

Note that the division by $\delta(\mathbf{p}, \Phi)$ in the case $\tilde{\ell}(\mathbf{p}, \Phi) < 0$ means that datasets are typically imbalanced, with negative values of $\mathcal{L}(\mathbf{p})$ showing absolute values much larger than those points with positive $\mathcal{L}(\mathbf{p})$, which is suboptimal for ML methods. We address this imbalance in Section III.

C. Models

Here, we focus on two well-known tight-binding models that have been shown to host FCIs, the first on the checkerboard lattice [12] and the second on the kagome lattice [44]. Their varying numbers of sublattices and connectivities produce distinct band geometries and interaction matrix elements, making them ideal for exploring universal versus model-specific FCI behavior.

The Hamiltonian we consider on the checkerboard lattice is

$$\begin{aligned} H &= H_{\text{kin}} + H_{\text{int}}, \\ H_{\text{kin}} &= - \sum_{\langle i,j \rangle} t_1 \exp(i\nu_{ij}\phi) c_i^\dagger c_j - \sum_{\langle\langle i,j \rangle\rangle} t_2 \nu_{ij} c_i^\dagger c_j + \sum_i M \mu_i n_i, \\ H_{\text{int}} &= V_1 \sum_{\langle i,j \rangle} :n_i n_j:, \end{aligned} \quad (6)$$

where c_i (c_i^\dagger) is the fermion annihilation (creation) operator at site i , $n_i = c_i^\dagger c_i$ is the density operator, and $: :$ indicates normal ordering. The nearest-neighbor (NN) and next-nearest-neighbor (NNN) sites are represented by $\langle i, j \rangle$, $\langle\langle i, j \rangle\rangle$. t_1 and ϕ parameterize the absolute value and phase of the NN hopping; t_2 parameterizes the purely real NNN hopping, with $\nu_{ij} = \pm 1$ encoding a chosen chirality for complex hoppings, as shown in Figure 1a; M is a mass term with alternating sign $\mu_i = \pm 1$ for different sublattices. Interactions are included through repulsive NN density-density terms with strength V_1 . Throughout, we set $V_1 = 1$ to fix the energy scale.

The second model, on the kagome lattice, has the same interaction Hamiltonian H_{int} as above but with the kinetic Hamiltonian given by

$$H_{\text{kin}} = - \sum_{\langle i,j \rangle} (t_1 + i\nu_{ij}\lambda_1) c_i^\dagger c_j - \sum_{\langle\langle i,j \rangle\rangle} (t_2 + i\nu_{ij}\lambda_2) c_i^\dagger c_j, \quad (7)$$

where t_1 and λ_1 parameterize the real and imaginary parts of the NN hopping, t_2 and λ_2 parameterize the real and imaginary parts of the NNN hopping, and $\nu_{ij} = \pm 1$ is a chirality chosen in the same convention as Figure 1b. As in the checkerboard model, we fix $V_1 = 1$.

Since we are entirely focused on the role of band geometry, we remove energy dispersion effects by flattening the lowest single-particle band and projecting the interactions to it, which effectively amounts to sending single-particle gaps to infinity without altering the band geometry [6]. In this projected regime, only the single-particle eigenstates enter the many-body calculation, so one may also set $t_1 = 1$ for both models. Consequently, the parameter spaces are three-dimensional (3D), $\mathbf{p}_{CB} = (\phi, t_2, M)$ for the checkerboard model and $\mathbf{p}_{KM} = (\lambda_1, t_2, \lambda_2)$ for the kagome model. Previous work [12, 44] has shown that the points around $\mathbf{p}_{CB} = (\pi/4, 1 - \sqrt{2}^{-1}, 0)$ and $\mathbf{p}_{KM} = (1, 0, 0)$ host FCI ground states. All ED calculations in our dataset are carried out at filling $\nu = 1/3$ of the lowest band. We use clusters with sizes $N_1 = 3, N_2 = 6$, since the resulting

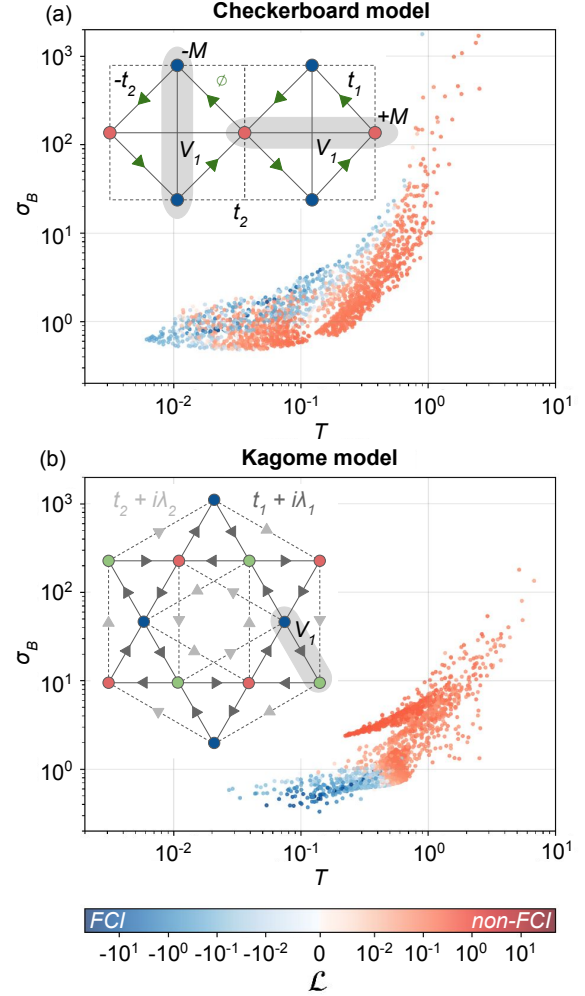


Figure 1. Log-log plots of the dataset used for ML analysis, representing the distribution of trace violation T and Berry curvature deviation σ_B , colored by the corresponding FCI quality metric \mathcal{L} . Data is generated from ED calculations using the Hamiltonian on (a) the checkerboard lattice (Eq. (6)) and (b) kagome lattice (Eq. (7)). Insets show a schematic representation of the lattice models, with arrows indicating hoppings with positive phase.

momentum grid includes all high-symmetry momentum points, and therefore our calculations can resolve competing orders such as charge density waves. For evaluations of the FCI quality metric, we sample the two extremal flux values $\{\Phi_j\} = \{0, \pi\}$.

D. Single-particle metrics

As inputs to our ML pipeline, we calculate two single-particle band-geometric quantities on the partially filled lowest band: the trace violation T between the Fubini–Study metric and Berry curvature, and the Berry curvature fluctuations σ_B

across the Brillouin zone (BZ). The quantum geometric tensor is

$$\eta_n^{\mu\nu}(\mathbf{k}) = \sum_n \langle \partial_{k_\mu} u_n(\mathbf{k}) | Q(\mathbf{k}) | \partial_{k_\nu} u_n(\mathbf{k}) \rangle, \quad (8)$$

where $u_n(\mathbf{k})$ is a cell-periodic Bloch state in band n and $Q(\mathbf{k}) = 1 - \sum_n |u_n(\mathbf{k})\rangle \langle u_n(\mathbf{k})|$. Its real and imaginary parts are the Fubini–Study metric and Berry curvature, respectively:

$$g_n^{\mu\nu}(\mathbf{k}) = \text{Re } \eta_n^{\mu\nu}(\mathbf{k}), \quad \mathcal{F}_n(\mathbf{k}) \varepsilon^{\mu\nu} = \frac{1}{2} \text{Im } \eta_n^{\mu\nu}(\mathbf{k}), \quad (9)$$

with $\varepsilon^{\mu\nu}$ the 2D Levi–Civita symbol. Finally, by focusing on the lowest band, the single-particle metrics of interest are defined as follows:

$$T = \frac{1}{2\pi} \int_{\text{BZ}} d^2k T(\mathbf{k}), \quad T(\mathbf{k}) = \text{Tr } g^{\mu\nu}(\mathbf{k}) - |\mathcal{F}(\mathbf{k})|, \quad (10)$$

$$\sigma_B = \sqrt{\int_{\text{BZ}} \frac{d^2k}{A_{\text{BZ}}} \left(\frac{\mathcal{F}(\mathbf{k})}{\mathcal{F}_0} - C \right)^2}.$$

where A_{BZ} is the BZ area, $\mathcal{F}_{\text{BZ}} = 2\pi/A_{\text{BZ}}$ and C the Chern number of the lowest band. Both quantities are normalized to be dimensionless and vanish for the lowest LL. We also include the band gap Δ as an input, which controls band mixing when compared to interaction scales and the bandwidth. However, because we work in the flattened projected limit, Δ is effectively sent to infinity as discussed previously, and therefore is irrelevant for the FCI stability. We shall see below that, although Δ is treated as an input, our ML method is able to detect its irrelevance.

Motivated by the algebra of projected density operators in LLs [29, 41], these geometric metrics are expected to serve as efficient surrogates for FCI stability, although in some cases their role has been challenged [36, 37, 42, 55–57]. The assembled dataset of paired geometric inputs and FCI quality labels $\{(T, \sigma_B, \Delta; \mathcal{L})\}$ constitute the dataset for our ML analysis. We note that, in general, the FCI quality metric cannot be expressed as a sole function of any collections of single-particle quantities. Our goal here instead is to quantitatively and systematically assess to what extent are T and σ_B reliable predictors of an FCI ground state in the parameter regions we study, and derive heuristic laws describing their relationship.

For the dataset, we focus on the behavior of \mathcal{L} near and within a region of parameter space where the ground state is an FCI. Therefore, we generate the data for each model by sampling parameter points in a 3-sphere centered at \mathbf{p}_{CB} and \mathbf{p}_{KM} , with radii chosen such that there is a roughly equal number of FCIs and non-FCIs in the dataset, i.e., points with $\mathcal{L}(\mathbf{p}) < 0$ and $\mathcal{L}(\mathbf{p}) > 0$, respectively. In Figure 1 we plot the datasets used for each model as a function of T and σ_B .

III. KOLMOGOROV–ARNOLD NETWORKS

A. Introduction

Neural networks (NNs) are a class of ML models designed to approximate complex, nonlinear mappings between inputs and outputs. The predictive capability of a NN arises from multiple compositions of linear transformations and nonlinear activation functions, the depth of which relates to its expressivity, i.e., the complexity of functions it can approximate. During training, the coefficients of these transformations are adjusted in order to minimize a user-defined loss function, which quantifies the discrepancy between predicted outputs and ground-truth values. Training typically proceeds via gradient-based optimization: the gradient of the loss with respect to each parameter is computed using backpropagation, and the parameters are iteratively updated in a direction that reduces the loss. This procedure enables the network to adapt its internal representation to capture the underlying functional relationship in the data.

Among the most fundamental architectures are multilayer perceptrons (MLPs). An MLP consists of a sequence of layers, each comprising multiple nodes. Denoting the inputs and outputs of the j -th node of a layer as \mathbf{x} and y_j , the computation performed at a node can be represented as:

$$y_j(\mathbf{x}) = \psi \left(\sum_i w_{ij} x_i + b_j \right), \quad (11)$$

where w_{ij} , b_j are the node’s weights and bias and $\psi(x)$ is a *fixed* nonlinear activation function. By stacking multiple such layers, an MLP is able to construct increasingly abstract feature representations, making it capable of approximating arbitrary continuous functions.

On the other hand, Kolmogorov–Arnold networks (KANs) [43] are a novel neural network architecture based on the Kolmogorov–Arnold representation theorem, which states that, under mild assumptions, a continuous multi-variable function $f(\mathbf{x})$ can be represented as a finite composition of continuous single-variable functions and additions:

$$f(\mathbf{x}) = \sum_q \Phi_q \left(\sum_p \phi_{q,p}(x_p) \right), \quad (12)$$

which can be seen as a 2-layer network parametrized by single-variable functions $(\Phi_q, \phi_{q,p})$. However, in general such functions can be pathological, which disallows gradient-based methods for function approximation. The KAN architecture instead employs multiple layers of smooth single-variable functions, which are then added or multiplied together at each node, and composed between layers as shown in Figure 2.

Intuitively, KANs can be understood as generalizations of MLPs, where the nonlinear activation functions are *trainable* rather than fixed. The activation functions $\psi(x)$ are parametrized as a combination of B-splines $B_i(x)$:

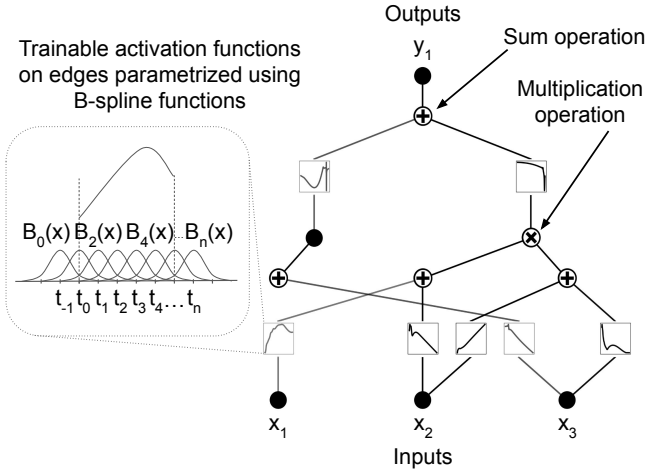


Figure 2. Example of a KAN [3,[1,1],1] architecture. In KAN notation, an architecture with n layers is described by a list of n entries, with the i -th entry specifying the number of addition nodes in the i -th layer. Layers with two numbers (i.e. [1,1]) indicate the number of additive and multiplicative nodes at that layer, respectively.

$$\psi(x) = \omega_b \frac{x}{1 + e^{-x}} + \omega_s \sum_i c_i B_i(x), \quad (13)$$

where the parameters c_i , ω_s and ω_b can be trained with standard backpropagation methods to fit any nonlinear relation.

The use of KANs in this work is motivated by their noticeable advantages over MLPs in terms of compactness and interpretability. While the typically high connectivity of MLPs hinder the extraction of general insights from the architecture, the trainable parameters in KANs are packaged within each edge rather than through increasing the network complexity, often leading to simpler networks for a given accuracy. Furthermore, KANs are trained with sparsity enforcement in the loss function followed by pruning, in which unnecessary edges and nodes are iteratively dropped from the network to reduce its size and complexity. This allows for fitting simple, single-variable functions to the nonlinear activation functions after training. This fitting procedure is typically done by choosing functions for each edge from a predetermined library of candidates, which can be compared through their R^2 values. Therefore, KANs allow for the integration of both NN-based predictions and symbolic regression into a single model, making it particularly useful for this problem, achieving both accurate prediction of \mathcal{L} as well as simple, interpretable symbolic formulas for its approximate dependence on (T, σ_B, Δ) . The full training process, which includes many design choices such as sparsity tuning, optimizer selection, specific training loss, hyperparameter tuning and pruning schedule, is crucial for achieving optimal results and is discussed in detail below and in Appendix A.

In order to evaluate the model performance on our FCI

dataset, we use the root mean square error (RMSE) and accuracy, defined as

$$\begin{aligned} \text{RMSE} &= \sqrt{\frac{1}{n} \sum_{i=1}^n (y_i - \hat{y}_i)^2}, \\ \text{Accuracy} &= \frac{\text{Correctly classified samples}}{\text{Total number of samples}}, \end{aligned} \quad (14)$$

where \hat{y}_i and y_i denote the ground-truth and predicted labels. “Correctly classified sample” is defined as the number of samples in which the sign of the FCI metric \mathcal{L} is predicted correctly by the KAN model.

The clear data trends in Figure 1, with distinct clusters for FCI and non-FCIs visible and reasonably low overlap, suggest that KAN models should be able to distinguish between the two classes using the input variables and simple symbolic functions alone.

B. Pipeline for formula extraction

We use a comprehensive pipeline to integrate the model training, evaluation, formula selection and final evaluation. The steps are the following, which are depicted visually in Figure 3a and expanded upon in Appendix A:

1. **Hyperparameter selection:** based on iterative tests and experimentation, a comprehensive set of hyperparameter values, including a range of possible architecture sizes, are selected to train multiple candidate KANs. These hyperparameters are chosen according to their performance in terms of prediction loss and accuracy, while favoring those architectures that offer the greatest network simplicity in terms of connectivity and compactness.
2. **Model evaluation:** once the models are trained, the best networks are chosen, with performance characterized by a balance between low RMSE, high accuracy and low network size.
3. **Candidate formula generation:** based on the selected models and a predetermined library of candidate functions, each of the models is adjusted to multiple formulas, with each edge having a high R^2 fit coefficient. The list of candidate formulas is then chosen to ensure high performance with the fewest and simplest candidate functions.
4. **Formula evaluation:** once the formulas are selected, we evaluate them on the regression and classification metrics. Out of the many possible candidates, a final representative for each model is selected, based on performance and formula simplicity.

We shall see that KANs are able to meet these stringent requirements for high accuracy, low network size and high sparsity, allowing for physically meaningful insights to be extracted from the final architectures through symbolic regression.

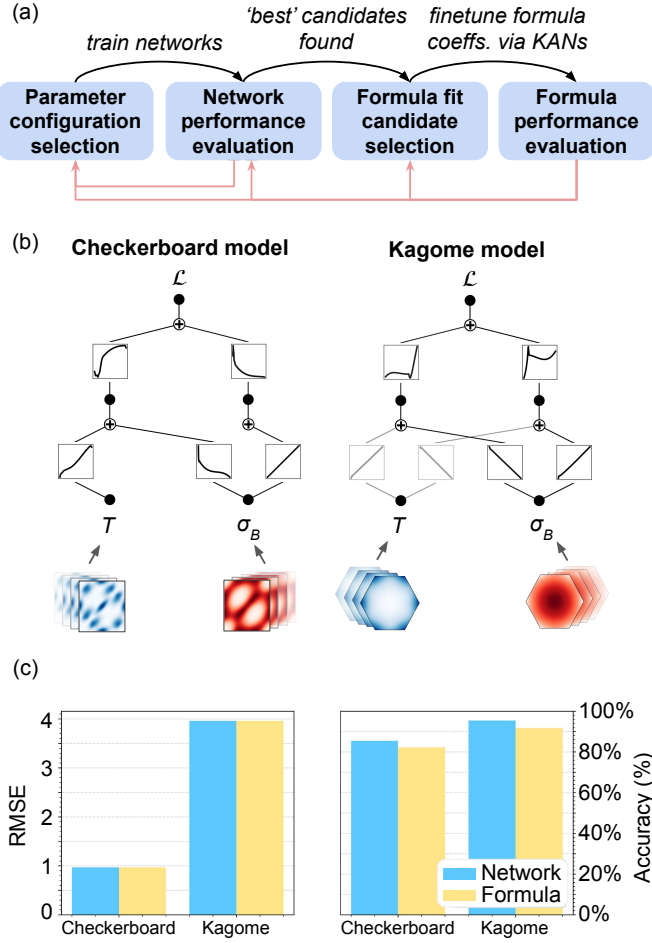


Figure 3. (a) ML pipeline for training KANs and extracting accurate symbolic formulas. (b) Representative KAN networks for the checkerboard and kagome models. The momentum-space functions $T(\mathbf{k})$ and $\mathcal{F}(\mathbf{k})$ (plotted respectively in blue and red, in each Brillouin zone) are used to compute T and σ_B , which are then fed into the networks as inputs, with output the FCI metric \mathcal{L} . (c) Regression and classification performance of networks and symbolic formulas, measured in terms of the RMSE and accuracy, respectively.

In Figure 3b we show illustrative KAN networks obtained after training, which capture the dependence of \mathcal{L} on band geometry.

IV. RESULTS

On training KANs on our FCI dataset, we first find that KANs effectively distinguish between relevant and irrelevant variables, systematically dropping the single-particle gap Δ whenever it was included as an input parameter. As discussed previously, in a band-projected ED calculation, any band mix-

ing effects are completely removed, and therefore Δ plays no direct role in determining the ground state, being relevant only insofar as it affects the distribution of $T(\mathbf{k})$ and $\mathcal{F}(\mathbf{k})$, which is already captured by T and σ_B .

Table I presents representative formulas and associated coefficients for each of the models. Although all of the expressions obtained are simple and interpretable, they are also accurate both in regression and classification metrics, as shown in Figure 3c. In particular, the KAN models and symbolic formulas for both lattice models scored above 80% in accuracy, even reaching above 90% for the kagome model. This is a testament to both the suitability of our KAN pipeline, as well as the predictive power of band-geometric properties in the likelihood and stability of an FCI ground state. The fact that the RMSEs show greater discrepancy between the models can be explained by noting the wider range of values of \mathcal{L} in the kagome model (Figure 1), which leads to larger errors due to outliers that amplify the overall mean. This aspect was partially mitigated with a sigmoid transformation performed within the training pipeline, which is detailed in Appendix A.

Overall, these formulas allow us to take the usual FCI heuristics one step further and quantitatively evaluate general trends of the FCI quality for each model. In the formula for the checkerboard model, \mathcal{L} is lowered, thereby resulting in a more stable FCI, if T is decreased but if σ_B is increased, although the functional dependencies are such that \mathcal{L} is far more sensitive to changes in T than to in σ_B . In contrast, the formula for the kagome model shows the same exponential dependence on both variables, such that an FCI ground state is favored if both T and σ_B are decreased. Although the specific functional dependencies on band geometry are formula-dependent and therefore not universal, in Appendix B we show that the general trends discussed above are consistent across formulas. The behavior of the checkerboard model, favoring increases in σ_B for more stable FCIs, is in contrast to the traditional expectation for FCIs, but it aligns with more recent work which has pointed out that a low σ_B can be irrelevant [37] or even detrimental [36] to the stability of an FCI. Here, we provide evidence for and partially recover these results in a purely data-driven manner.

Finally, the intrinsic exponential complexity of ED calculations typically hinders the generation of sizable, high-quality datasets. This motivates us to assess the performance of KANs in data-scarce scenarios. We do so by training KANs on a small set of sampled points with the same distribution of FCIs and non-FCIs, and testing the performance of the final network and symbolic expressions on unseen data. As shown in Figure 4, the regression and classification metrics remain robust for small datasets, with performance on the kagome model largely unchanged down to as few as $\sim 10^2$ ED spectra. These trends demonstrate that KANs retain strong predictive power in data-scarce settings, delivering stable statistical metrics without requiring a large number of data points.

Model	Formula	Params
Checkerboard	$\mathcal{L}(T, \sigma_B) = -w_0 + w_1 T + (w_2 \sigma_B + w_3)^{-1}$	$w_0 = 0.461, w_1 = 0.765, w_2 = 0.454, w_3 = 2.010$
Kagome	$\mathcal{L}(T, \sigma_B) = w_0 - w_1 \exp(-w_2 T) - w_3 \exp(-w_4 \sigma_B)$	$w_0 = 0.112, w_1 = 0.175, w_2 = 4.109, w_3 = 0.311, w_4 = 1.542$

Table I. Representative formulas for the FCI metric \mathcal{L} as a function of single-particle band geometric quantities, with learned parameters w_i also shown.

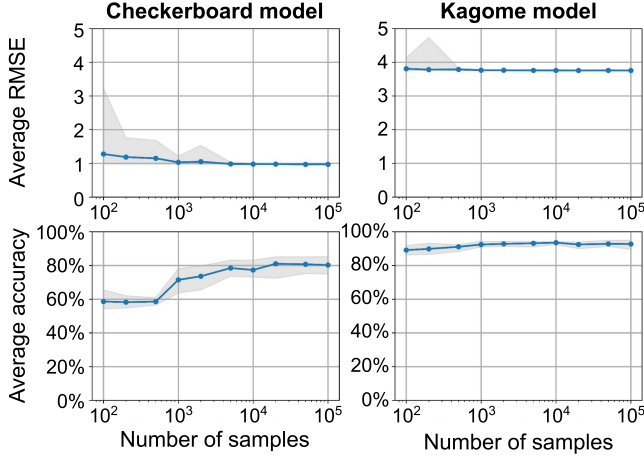


Figure 4. Average RMSEs and accuracies as a function of training dataset size, with error bars in grey.

V. CONCLUSIONS

In this work, we have addressed a key challenge in the study of fractional Chern insulators (FCIs) using a data-driven approach: developing interpretable and quantitative heuristics that link single-particle band geometry to FCI stability. To achieve this, we combined large-scale exact diagonalization with a physically motivated FCI metric \mathcal{L} [42] and interpretable machine learning via Kolmogorov–Arnold networks (KANs) [43]. This pipeline allowed us to extract symbolic formulas that connect the trace violation T and Berry curvature fluctuations σ_B to FCI stability.

Our results show that remarkably simple formulas for \mathcal{L} involving only T and σ_B can predict whether an FCI is the ground state of the system and quantitatively capture its stability, with high accuracy across two representative models on the checkerboard and kagome lattices. Both models exhibit strong nonlinear but learnable relationships in the (T, σ_B) plane, with the extracted formulas achieving over 80% classification accuracy and competitive regression performance. Interestingly, we find model-dependent trends: while large σ_B is detrimental to stability in the kagome model, it plays a stabilizing role in the checkerboard lattice, in line with recent theoretical results [36, 37]. Therefore, KANs were able to surface unusual trends in the stability dependence on σ_B in a purely data-driven approach, without the need for fine-tuned models where T and σ_B can be separately controlled. The extracted symbolic expressions also offer insights into the ground state of these quantum

systems and the crucial role of single-particle physics, delivering accurate and predictive results even for small-scale datasets, a crucial requirement in numerical many-body physics.

Looking ahead, this framework provides a general methodology for exploring and discovering complex dependencies of many-body states on arbitrary physical quantities. Our findings illustrate the unique potential of KANs and ML in accelerating exploration in the physical sciences through hypothesis formulation and testing.

VI. ACKNOWLEDGEMENTS

We thank Zhuo Chen and Patrick J. Ledwith for stimulating discussions. We acknowledge support from the National Science Foundation under Cooperative Agreement PHY-2019786 (The NSF AI Institute for Artificial Intelligence and Fundamental Interactions). O.M.C. acknowledges the CFIS Mobility Program for its support, particularly Fundació Privada Mir-Puig, CFIS partners, and donors of the crowdfunding program. A.G.F. acknowledges support from the Whiteman Fellowship and the Surpina and Panos Eurnekian Nanotechnology Fund Fellowship. S.V. and M.S. acknowledge support from the U.S. Office of Naval Research (ONR) Multidisciplinary University Research Initiative (MURI) under Grant No. N00014-20-1-2325 on Robust Photonic Materials with Higher-Order Topological Protection. This material is based upon work also supported in part by the U. S. Army Research Office through the Institute for Soldier Nanotechnologies at MIT, under Collaborative Agreement Number W911NF-23-2-0121. The MIT SuperCloud and Lincoln Laboratory Supercomputing Center provided computing resources that contributed to the results reported in this work.

VII. APPENDIX A: TRAINING PIPELINE DETAILS

Here we detail the training process, including choices of optimizer, hyperparameters and initial KAN architectures. As is typical in ML problems, such choices are essential to achieve optimal model performance. The following configuration was used to train the final models within PyTorch:

- **AdamW optimizer** with the default configuration.
- **smoothL1 loss** over N samples: $\mathcal{L} = \frac{1}{N} \sum_{i=1}^N L(\hat{y}_i, y_i)$,

Model	Formula	Params	RMSE	Acc.
Checkerboard	$\mathcal{L} = w_0 - (w_1 T + w_2)^{-1} + (w_3 \sigma_B + w_4)^{-1}$	$w_0 = 1.157, w_1 = 0.317, w_2 = 0.617, w_3 = 0.489, w_4 = 2.007$	0.98	83.19 %
	$\mathcal{L} = w_0 - (w_1 T + w_2)^{-1} + w_3 \exp(-w_4 \sigma_B)$	$w_0 = 1.237, w_1 = 0.321, w_2 = 0.617, w_3 = 0.399, w_4 = 0.194$	0.98	81.78 %
Kagome	$\mathcal{L} = w_0 - w_1 \exp(-w_2 T) - (w_3 \sigma_B - w_4)^{-1}$	$w_0 = 0.129, w_1 = 0.175, w_2 = 4.091, w_3 = 12.967, w_4 = 0.913$	3.91	91.66 %

Table II. Additional formulas for the FCI metric \mathcal{L} as a function of single-particle band geometric quantities, and associated learned parameters w_i , RMSE and accuracies.

where

$$L(\hat{y}, y) = \begin{cases} 0.5(\hat{y} - y)^2, & \text{if } |\hat{y} - y| < 1 \\ |\hat{y} - y| - 0.5, & \text{otherwise} \end{cases}$$

- **120 training epochs** with pruning every 20 epochs.
- **Exponential decay scheduler** with starting learning rate $lr = 5 \times 10^{-3}$ and weight decay $\gamma = 0.98$.

For data sampling and transformation, we chose:

- **10^5 training samples** extracted from each dataset, with 2×10^4 validation samples and 10^5 test samples for a uniform final evaluation.
- **10^3 samples per batch**, for a total of 10^2 batches per epoch.
- **Metric transformation:** In order to address the wide data range of FCI metrics, we applied the transformation $\mathcal{L}' = 2 \sigma(a\mathcal{L}) - 1$, mapping the metric to the range $\mathcal{L}' \in (-1, 1)$. This transformation was performed on the predicted and ground-truth values *after* the prediction. After experimentation, the value for $a = 20$ was chosen for both the kagome and checkerboard models, based on an ablation study performed on the variable.
- **Uniform sampling:** samples were binned according to their transformed value for the FCI metric into 10^2 different bins, with a roughly equal amount of samples selected from each bin to avoid oversampling some regions of the (T, σ_B) plane.

The KAN-specific choices of architecture and hyperparameters were:

- **Architecture:** we initialized KANs using the following sizes: $[2,1]$; $[2,2,1]$; $[2,5,1]$; $[2,[2,2],1]$; $[2,2,2,1]$; $[2,[2,2],[2,2],1]$; $[2,5,5,1]$; $[2,[2,2],[2,2],[2,2],1]$; $[2,10,1]$; $[2,10,10,1]$.
- **Sparsity configuration:** 3 configurations were tested, introducing sparsity to the network at different rates (see definition of coefficients in [43]):

1. $\lambda = 10^{-3}$, $\lambda_e = 0.1$, $\lambda_{coeffdif} = 0.1$, $\lambda_{l1} = 0.1$, $\lambda_{coef} = 0.01$
2. $\lambda = 5 \cdot 10^{-3}$, $\lambda_e = 0.25$, $\lambda_{coeffdif} = 0.25$, $\lambda_{l1} = 0.2$, $\lambda_{coef} = 0.01$
3. $\lambda = 10^{-2}$, $\lambda_e = 0.5$, $\lambda_{coeffdif} = 0.5$, $\lambda_{l1} = 0.4$, $\lambda_{coef} = 0.01$

- **KAN model parameters:** we initialized KANs with the following set of parameters:

- **Grid size:** 20
- **k :** 3
- **grid $_{\epsilon}$:** 0.01

For the symbolic regression part, a list of possible candidate functions was selected to be used when fitting each edge. After multiple rounds of evaluation considering the complexity and performance of the different candidates, the final list contained the following single-variable functions: x , x^2 , x^3 , $\frac{1}{x}$, e^x and 0, which we have found to be sufficient for providing meaningful and accurate expressions.

For each edge, these formulas were fitted to the trained non-linear activation by tuning the affine parameters, and then compared through their R^2 value, where

$$R^2 = \frac{\sum_i (\hat{y}_i - \bar{y})^2}{\sum_i (y_i - \bar{y})^2}. \quad (15)$$

A threshold of 0.95 for the R^2 values was used, with all candidates above that value considered for each edge. If none were above the threshold, only the single best function was considered. All possible candidate combinations were considered in the final step, in which the formula quality was evaluated.

VIII. APPENDIX B: ADDITIONAL METRIC FORMULAS

In Table II we show additional symbolic formulas generated for each model through the KAN pipeline, along with their statistical metrics. We note that, although the specific functions can vary depending on training details, they all show similar trends and dependencies.

[1] R. B. Laughlin, Anomalous Quantum Hall Effect: An Incompressible Quantum Fluid with Fractionally Charged Excitations,

Phys. Rev. Lett. **50**, 1395 (1983).

- [2] F. D. M. Haldane, Fractional quantization of the Hall effect: A hierarchy of incompressible quantum fluid states, *Phys. Rev. Lett.* **51**, 605 (1983).
- [3] V. L. Pokrovsky and A. L. Talapov, A simple model for fractional Hall effect, *Journal of Physics C: Solid State Physics* **18**, L691 (1985).
- [4] S. A. Trugman and S. Kivelson, Exact results for the fractional quantum Hall effect with general interactions, *Phys. Rev. B* **31**, 5280 (1985).
- [5] S. A. Parameswaran, R. Roy, and S. L. Sondhi, Fractional quantum hall physics in topological flat bands, *C. R. Phys.* **14**, 816 (2013).
- [6] E. J. Bergholtz and Z. Liu, Topological Flat Band Models and Fractional Chern Insulators, *Int. J. Mod. Phys. B* **27**, 1330017 (2013).
- [7] Z. Liu and E. J. Bergholtz, Recent Developments in Fractional Chern Insulators (2024) pp. 515–538, arXiv:2208.08449.
- [8] T. Neupert, L. Santos, C. Chamon, and C. Mudry, Fractional quantum Hall states at zero magnetic field, *Phys. Rev. Lett.* **106**, 236804 (2011).
- [9] K. Sun, Z. Gu, H. Katsura, and S. Das Sarma, Nearly flatbands with nontrivial topology, *Phys. Rev. Lett.* **106**, 236803 (2011).
- [10] E. Tang, J.-W. Mei, and X.-G. Wen, High-Temperature Fractional Quantum Hall States, *Phys. Rev. Lett.* **106**, 236802 (2011).
- [11] D. N. Sheng, Z.-C. Gu, K. Sun, and L. Sheng, Fractional quantum Hall effect in the absence of Landau levels, *Nat. Commu.* **2**, 389 (2011).
- [12] N. Regnault and B. A. Bernevig, Fractional Chern Insulator, *Phys. Rev. X* **1**, 021014 (2011).
- [13] M. Hafezi, A. S. Sørensen, E. Demler, and M. D. Lukin, Fractional quantum Hall effect in optical lattices, *Phys. Rev. A* **76**, 023613 (2007).
- [14] Y.-F. Wang, Z.-C. Gu, C.-D. Gong, and D. N. Sheng, Fractional Quantum Hall Effect of Hard-Core Bosons in Topological Flat Bands, *Phys. Rev. Lett.* **107**, 146803 (2011).
- [15] E. M. Spanton, A. A. Zibrov, H. Zhou, T. Taniguchi, K. Watanabe, M. P. Zaletel, and A. F. Young, Observation of fractional Chern insulators in a van der Waals heterostructure, *Science* **360**, 62 (2018).
- [16] Y. Xie, A. T. Pierce, J. M. Park, D. E. Parker, E. Khalaf, P. Ledwith, Y. Cao, S. H. Lee, S. Chen, P. R. Forrester, *et al.*, Fractional Chern insulators in magic-angle twisted bilayer graphene, *Nature* **600**, 439 (2021).
- [17] H. Park, J. Cai, E. Anderson, Y. Zhang, J. Zhu, X. Liu, C. Wang, W. Holtzmann, C. Hu, Z. Liu, T. Taniguchi, K. Watanabe, J.-H. Chu, T. Cao, L. Fu, W. Yao, C.-Z. Chang, D. Cobden, D. Xiao, and X. Xu, Observation of fractionally quantized anomalous Hall effect, *Nature* **622**, 74 (2023).
- [18] Y. Zeng, Z. Xia, K. Kang, J. Zhu, P. Knüppel, C. Vaswani, K. Watanabe, T. Taniguchi, K. F. Mak, and J. Shan, Thermodynamic evidence of fractional chern insulator in moiré mote2, *Nature* **622**, 69 (2023).
- [19] Z. Lu, T. Han, Y. Yao, A. P. Reddy, J. Yang, J. Seo, K. Watanabe, T. Taniguchi, L. Fu, and L. Ju, Fractional quantum anomalous Hall effect in multilayer graphene, *Nature* **626**, 759 (2024).
- [20] J. Xie, Z. Huo, X. Lu, Z. Feng, Z. Zhang, W. Wang, Q. Yang, K. Watanabe, T. Taniguchi, K. Liu, *et al.*, Tunable fractional Chern insulators in rhombohedral graphene superlattices, *Nature Materials*, 1 (2025).
- [21] Z. Lu, T. Han, Y. Yao, Z. Hadjri, J. Yang, J. Seo, L. Shi, S. Ye, K. Watanabe, T. Taniguchi, *et al.*, Extended quantum anomalous Hall states in graphene/hbn moiré superlattices, *Nature* **637**, 1090 (2025).
- [22] S. H. Aronson, T. Han, Z. Lu, Y. Yao, J. P. Butler, K. Watanabe, T. Taniguchi, L. Ju, and R. C. Ashoori, Displacement field-controlled fractional Chern insulators and charge density waves in a graphene/hBN moiré superlattice, *Physical Review X* **15**, 031026 (2025).
- [23] J. Cai, E. Anderson, C. Wang, X. Zhang, X. Liu, W. Holtzmann, Y. Zhang, F. Fan, T. Taniguchi, K. Watanabe, *et al.*, Signatures of fractional quantum anomalous hall states in twisted MoTe2, *Nature* **622**, 63 (2023).
- [24] F. Xu, Z. Sun, T. Jia, C. Liu, C. Xu, C. Li, Y. Gu, K. Watanabe, T. Taniguchi, B. Tong, J. Jia, Z. Shi, S. Jiang, Y. Zhang, X. Liu, and T. Li, Observation of integer and fractional quantum anomalous Hall effects in twisted bilayer mote2, *Phys. Rev. X* **13**, 031037 (2023).
- [25] Z. Ji, H. Park, M. E. Barber, C. Hu, K. Watanabe, T. Taniguchi, J.-H. Chu, X. Xu, and Z.-X. Shen, Local probe of bulk and edge states in a fractional Chern insulator, *Nature* **635**, 578 (2024).
- [26] E. Redekop, C. Zhang, H. Park, J. Cai, E. Anderson, O. Sheekey, T. Arp, G. Babikyan, S. Salters, K. Watanabe, *et al.*, Direct magnetic imaging of fractional chern insulators in twisted mote2 with a superconducting sensor, arXiv preprint arXiv:2405.10269 (2024).
- [27] F. Xu, Z. Sun, J. Li, C. Zheng, C. Xu, J. Gao, T. Jia, K. Watanabe, T. Taniguchi, B. Tong, *et al.*, Signatures of unconventional superconductivity near reentrant and fractional quantum anomalous Hall insulators, arXiv preprint arXiv:2504.06972 (2025).
- [28] A.-K. Wu, L. Primeau, J. Zhang, K. Sun, Y. Zhang, and S.-Z. Lin, Modeling quantum geometry for fractional Chern insulators with unsupervised learning, arXiv:2510.03018 (2025).
- [29] R. Roy, Band geometry of fractional topological insulators, *Phys. Rev. B* **90**, 165139 (2014).
- [30] T. S. Jackson, G. Möller, and R. Roy, Geometric stability of topological lattice phases, *Nat Commun* **6**, 8629 (2015).
- [31] C. H. Lee, M. Claassen, and R. Thomale, Band structure engineering of ideal fractional chern insulators, *Phys. Rev. B* **96**, 165150 (2017).
- [32] P. J. Ledwith, G. Tarnopolsky, E. Khalaf, and A. Vishwanath, Fractional chern insulator states in twisted bilayer graphene: An analytical approach, *Phys. Rev. Res.* **2**, 023237 (2020).
- [33] T. Ozawa and B. Mera, Relations between topology and the quantum metric for Chern insulators, *Phys. Rev. B* **104**, 045103 (2021).
- [34] B. Mera and T. Ozawa, Kähler geometry and chern insulators: Relations between topology and the quantum metric, *Phys. Rev. B* **104**, 045104 (2021).
- [35] J. Wang, J. Cano, A. J. Millis, Z. Liu, and B. Yang, Exact landau level description of geometry and interaction in a flatband, *Phys. Rev. Lett.* **127**, 246403 (2021).
- [36] D. Varjas, A. Abouelkomsan, K. Yang, and E. J. Bergholtz, Topological lattice models with constant Berry curvature, *SciPost Phys.* **12**, 118 (2022).
- [37] P. J. Ledwith, A. Vishwanath, and D. E. Parker, Vortexability: A unifying criterion for ideal fractional Chern insulators, *Phys. Rev. B* **108**, 205144 (2023).
- [38] B. Estienne, N. Regnault, and V. Crépel, Ideal chern bands as landau levels in curved space, *Phys. Rev. Res.* **5**, L032048 (2023).
- [39] N. Okuma, Constructing vortex functions and basis states of chern insulators: Ideal condition, inequality from index theorem, and coherentlike states on the von neumann lattice, *Phys. Rev. B*

- 110**, 245112 (2024).
- [40] J. Shi, J. Cano, and N. Morales-Durán, Effects of Berry curvature on ideal band magnetorotons, [arXiv preprint arXiv:2503.15900](#) (2025).
 - [41] S. M. Girvin, A. H. MacDonald, and P. M. Platzman, Magneto-roton theory of collective excitations in the fractional quantum Hall effect, *Phys. Rev. B* **33**, 2481 (1986).
 - [42] A. G. Fonseca, E. Wang, S. Vaidya, P. J. Ledwith, A. Vishwanath, and M. Soljačić, Gradient-based search of quantum phases: discovering unconventional fractional Chern insulators, [arXiv preprint arXiv:2509.10438](#) (2025).
 - [43] Z. Liu, Y. Wang, S. Vaidya, F. Ruehle, J. Halverson, M. Soljačić, T. Y. Hou, and M. Tegmark, KAN: Kolmogorov-Arnold networks, [arXiv preprint arXiv:2404.19756](#) (2024).
 - [44] Y.-L. Wu, B. A. Bernevig, and N. Regnault, Zoology of fractional Chern insulators, *Phys. Rev. B* **85**, 075116 (2012).
 - [45] A. Abouelkomsan, Z. Liu, and E. J. Bergholtz, Particle-hole duality, emergent Fermi liquids, and fractional Chern insulators in moiré flatbands, *Phys. Rev. Lett.* **124**, 106803 (2020).
 - [46] C. Repellin and T. Senthil, Chern bands of twisted bilayer graphene: Fractional Chern insulators and spin phase transition, *Phys. Rev. Res.* **2**, 023238 (2020).
 - [47] P. Wilhelm, T. C. Lang, and A. M. Läuchli, Interplay of fractional chern insulator and charge density wave phases in twisted bilayer graphene, *Phys. Rev. B* **103**, 125406 (2021).
 - [48] V. Crépel and L. Fu, Anomalous Hall metal and fractional Chern insulator in twisted transition metal dichalcogenides, *Phys. Rev. B* **107**, L201109 (2023).
 - [49] Z. Liu, A. Abouelkomsan, and E. J. Bergholtz, Gate-tunable fractional Chern insulators in twisted double bilayer graphene, *Phys. Rev. Lett.* **126**, 026801 (2021).
 - [50] H. Li, U. Kumar, K. Sun, and S.-Z. Lin, Spontaneous fractional Chern insulators in transition metal dichalcogenide moiré superlattices, *Phys. Rev. Res.* **3**, L032070 (2021).
 - [51] A. P. Reddy, F. Alsallom, Y. Zhang, T. Devakul, and L. Fu, Fractional quantum anomalous hall states in twisted bilayer MoTe_2 and WSe_2 , *Phys. Rev. B* **108**, 085117 (2023).
 - [52] B. A. Bernevig and N. Regnault, Emergent many-body translational symmetries of Abelian and non-Abelian fractionally filled topological insulators, *Phys. Rev. B* **85**, 075128 (2012).
 - [53] E. Ardonne, E. J. Bergholtz, J. Kailasvuori, and E. Wikberg, Degeneracy of non-Abelian quantum Hall states on the torus: domain walls and conformal field theory, *J. Stat. Mech.* **2008**, P04016 (2008).
 - [54] M. Oshikawa, Commensurability, excitation gap, and topology in quantum many-particle systems on a periodic lattice, *Phys. Rev. Lett.* **84**, 1535 (2000).
 - [55] S. H. Simon, F. Harper, and N. Read, Fractional Chern insulators in bands with zero Berry curvature, *Phys. Rev. B* **92**, 195104 (2015).
 - [56] W. Yang, D. Zhai, T. Tan, F.-R. Fan, Z. Lin, and W. Yao, Fractional quantum anomalous Hall effect in a singular flat band, *Phys. Rev. Lett.* **134**, 196501 (2025).
 - [57] Z. Lin, W. Yang, H. Lu, D. Zhai, and W. Yao, Fractional Chern insulator states in an isolated flat band of zero Chern number, [arXiv:2505.09009](#) (2025).